Synthesis, Crystal and Electronic Structures, Magnetic and Electrical Transport Properties of Bismuthides $NdZn_{0.6}Bi_2$ and $(La_{0.5}RE_{0.5})Zn_{0.6}Bi_2$ (RE=Pr, Nd)

Karishma Prasad [a], Dinesh Upreti [b], Md Rafique Un Nabi [b], Richeal A Oppong [d], Fei Wang [e], Manish Shinde [f], Jin Hu [b, c, *], Jian Wang [a, *]

[a] *Department of Chemistry and Biochemistry, Wichita State University, Wichita, Kansas 67260, United States*

[b] *Department of Physics, University of Arkansas, Fayetteville, Arkansas 72701, United States*

[c] *Materials Science and Engineering Program, Institute for Nanoscience and Engineering, University of Arkansas, Fayetteville, Arkansas 72701, United States*

[d] *Department of Chemistry, Iowa State University, Ames, Iowa 50011, United States*

[e] *Department of Chemistry, Missouri State University, Springfield, Missouri, 65897, United States*

[f] *National Institute for Aviation Research, Wichita State University, Wichita, Kansas 67260, United States*

Abstract

Bismuth is a good constituent element for many quantum materials due to its large atomic number, the $6s^2 6p^3$ orbitals, and strong spin-orbital coupling. In this work, three new bismuthides $NdZn_{0.6}Bi_2$, $(La_{0.5}Pr_{0.5})Zn_{0.6}Bi_2$, and $(La_{0.5}Nd_{0.5})Zn_{0.6}Bi_2$ were grown by a metal flux method and their crystal structures were accurately determined by single crystal X-ray diffraction. These new bismuthides belong to the RE-T-Pn_2 (RE=La-Lu, T=Mn, Fe, Co, Ni, Zn, Pn=P, As, Sb, Bi) family, which are isostructural and crystallize in the $HfCuSi_2$ structure type. The bismuth elements have two possible oxidation states of Bi^{3-} and Bi^-, which were studied by X-ray photoelectron spectroscopy (XPS). Two binding energy peaks of 155.91 eV and 161.23 eV were observed for Bi atoms within $NdZn_{0.6}Bi_2$, and similar binding energy peaks were detected in NdBi and LiBi. XPS also confirmed the trivalent nature of Nd, which was further verified by magnetic measurements. Additionally, magnetic measurements found that $NdZn_{0.6}Bi_2$ exhibits an antiferromagnetic transition around 3K, while the mixed-cation compounds do not show any magnetic transition down to 2K. Electronic transport measurements reveal weak magnetoresistance in all three compounds, with a maximum value of 25% at 2K and 9T for $(La_{0.5}Nd_{0.5})Zn_{0.6}Bi_2$.

Introduction

Zintl compounds, which were named after Eduard Zintl due to his significant contributions, have remained at the forefront of solid-state chemistry research for many decades [1-11]. The comprehensive interplay between crystal structure, chemical bonding, and electronic structure within Zintl compounds is the 'double-edged sword' for solid-state chemists, which leads to intriguing physical properties, but it adds complexity [12-18]. The typical Zintl compounds constitute elements from the left side of the periodic table such as alkali metals or alkali earth metals as "electron donors" and elements from the right side of the periodic table such as groups 13–16 as "electron acceptors". Generally, Zintl compounds are valence compounds. When electrons from electropositive elements are deficient, the anions would form homoatomic bonds to compensate for the electron deficiency. The study of the Zintl compounds fostered an important concept of the Zintl-Klemm concept. The Zintl-Klemm concept states that the valence electrons are transferred from the more electropositive to the more electronegative atoms within the crystal lattice, where the more electronegative polyanions are isostructural to the structural motifs of isoelectronic elements. The Zintl-Klemm concept was widely employed to interpret the nature of bonding of and electronic properties of the Zintl compounds and even expanded to many polar intermetallic compounds [19-23].

Zintl compounds are a subgroup of intermetallic compounds. The boundary of Zintl compounds has been heavily expanded after intensive research [24-40]. Among many Zintl compounds and polar intermetallic compounds, bismuth-contained compounds are very interesting to us. Bismuth is the heaviest non-radioactive element. Owing to its large atomic number and the $6s^2 6p^3$ orbitals, bismuth is a good constituent element for many quantum materials due to the presence of strong spin-orbit coupling [41-43]. In this work, we report the synthesis, crystal and electronic structures, and magnetic properties of three new bismuthides $NdZn_{0.6}Bi_2$ and $(La_{0.5}RE_{0.5})Zn_{0.6}Bi_2$ (RE=Pr, Nd). The newly discovered compounds belong to the RE-T-Pn_2 (RE=La-Lu, T=Zn, Ni, Fe, etc., Pn=P, As, Sb, Bi) family [44-70]. One interesting observation would be there were 33 Sb-based compounds reported within the RE-T-Pn_2 family, compared to only 7 known Bi-based compounds discovered according to the ICSD 2023-2 database. Due to the presence of rare earth elements, transition metals, and Bi square nets, the study of the RE-T-Bi_2 system might result in intriguing materials. The RE-T-Pn_2 family can be cataloged into polar intermetallic compounds. The Zintl-

Klemm concept can be utilized to understand the bonding pictures and predicate the physical properties of the RE-T-Pn_2 family, which was showcased in this work.

Experimental Details

Synthesis: All reactants were stored and operated in an argon-filled glovebox with an oxygen level below 0.5 ppm. All starting materials were commercial grade and used as received: Bi pieces (Fisher Scientific, 99.99%), La powder (ESPI Metals, 99.7%), Nd powder (ESPI Metals, 99.8%), Pr powder (ESPI Metals, 99.7%), and Zn granules (Fisher Scientific, 99.8%).

The crystals of $NdZn_{0.6}Bi_2$, $(La_{0.5}Pr_{0.5})Zn_{0.6}Bi_2$, and $(La_{0.5}Nd_{0.5})Zn_{0.6}Bi_2$ were grown by employing a self-flux growth method using Zn-Bi flux. Stoichiometric ratio of RE:Zn: Bi = 1:12:20 was used for synthesizing $NdZn_{0.6}Bi_2$. For mixed-cation samples $(La_{0.5}Pr_{0.5})Zn_{0.6}Bi_2$ and $(La_{0.5}Nd_{0.5})Zn_{0.6}Bi_2$, La:RE:Zn:Bi = 0.5:0.5:12:20 were used. The reactants were placed in an evacuated fused-silica tube, heated to 900 °C for 10 hours, annealed at this temperature for 48 hours, and cooled to 600 °C at a rate of 3 °C/h. At 600 °C, Zn and Bi flux was removed via centrifuge. Plate-shaped silver color single crystals were obtained. These obtained crystals were found to be sensitive to air and moisture.

Lab powder X-ray Diffraction: Due to the air instability of $NdZn_{0.6}Bi_2$, $(La_{0.5}Pr_{0.5})Zn_{0.6}Bi_2$, and $(La_{0.5}Nd_{0.5})Zn_{0.6}Bi_2$, air-sensitive holders were utilized to run data collection using a Rigaku Mini Flex 6G diffractometer with Cu-Kα radiation (λ =1.5406 Å). A scan range of 2θ = 10° – 40° was used to avoid the strong peaks coming from Be holder, with a scan step of 0.04° and fifteen seconds of exposure time.

Single Crystal X-ray Diffraction: The sample preparation for single crystal X-ray diffraction was carried in a glovebox. Selected crystals were covered in Paratone oil and quickly transferred to a diffractometer equipped with liquid N_2. Single crystal diffraction experiments were carried out at 173 K using a Bruker D8 Venture diffractometer with a Bruker Photon100 CMOS detector employing Mo-Kα radiation. All datasets were integrated using the Bruker SAINT software package [71]. The strong absorption of bismuth should take into account. In this work, a "multi-scan" absorption correction method was employed. The solution and refinement of the crystal structures were carried out using the SHELX suite of programs [72]. The refinement of $NdZn_{0.6}Bi_2$ found the partial occupancy of Zn sites of occupancy of 61(3)%, which resulted in an experimental formula

of $NdZn_{0.56}Bi_2$. The occupancy of Zn sites were determined to be 60.5(2)% and 57.8(1)% for $(La_{0.5}Pr_{0.5})Zn_{0.6}Bi_2$ and $(La_{0.5}Nd_{0.5})Zn_{0.6}Bi_2$, respectively. The refinement of occupancy of La/Pr and La/Nd atom pairs is challenging due to their comparable atomic numbers. Energy dispersive spectrum (EDS) verified the atomic ratio of La/Pr and La/Nd is close to 1:1 (**Table S1**), which agrees well with the ratio of source materials for crystal growth as stated above. Because the occupancy of Zn for all three samples is close to 60%, chemical formulas of $NdZn_{0.6}Bi_2$, $(La_{0.5}Pr_{0.5})Zn_{0.6}Bi_2$, and $(La_{0.5}Nd_{0.5})Zn_{0.6}Bi_2$ are used in this work. Details of the data collection and structure refinement are provided in **Table 1**. Atomic coordinates and selected bond distances are listed in **Tables S2** and **S3**. Crystallographic data for $NdZn_{0.6}Bi_2$, $(La_{0.5}Pr_{0.5})Zn_{0.6}Bi_2$, and $(La_{0.5}Nd_{0.5})Zn_{0.6}Bi_2$ have been deposited to the Cambridge Crystallographic Data Centre, CCDC, 12 Union Road, Cambridge CB21EZ, UK. Copies of the data can be obtained free of charge by quoting the depository numbers CCDC- 2366796 ($NdZn_{0.6}Bi_2$), CCDC- 2366795 ($(La_{0.5}Pr_{0.5})Zn_{0.6}Bi_2$), and CCDC- 2366794 ($(La_{0.5}Nd_{0.5})Zn_{0.6}Bi_2$).

Table 1. Selected crystal data and structure refinement parameters for $NdZn_{0.6}Bi_2$, $(La_{0.5}Pr_{0.5})Zn_{0.6}Bi_2$, and $(La_{0.5}Nd_{0.5})Zn_{0.6}Bi_2$.

Compounds	1	2	3
Experimental Formula	$NdZn_{0.56}Bi_2$	$(La_{0.17}Pr_{0.83})Zn_{0.61}Bi_2$	$(La_{0.50}Nd_{0.50})\ Zn_{0.60}Bi_2$
Designated Formula	$NdZn_{0.6}Bi_2$	$(La_{0.5}Pr_{0.5})Zn_{0.6}Bi_2$	$(La_{0.50}\ Nd_{0.50})\ Zn_{0.6}Bi_2$
Formula weight	599.13	598.08	598.76
Temperature	173(2) K		
Radiation, wavelength	Mo Kα, 0.71073 Å		

Crystal system	Tetragonal		
Space group	*P*4/*nmm* (No.129)		
a(Å)	4.53190(14)	4.5636(2)	4.5616(2)
c(Å)	9.7060(6)	9.8797(7)	9.8539(6)
Z	2	2	2
V(Å^3)	199.343(17)	205.76(2)	205.04(2)
D_c(g cm^{-3})	9.982	9.653	9.698
μ (mm^{-1})	103.952	99.913	100.142
R_1,	0.0595	0.0273	0.0190
wR_2 (I > 2σ(I))	0.1347	0.0619	0.0397
R_1,	0.0617	0.0293	0.0206
wR_2 (all data)	0.1534	0.0751	0.0527

Elemental Analysis: Elemental analysis of $NdZn_{0.6}Bi_2$, $(La_{0.5}Pr_{0.5})Zn_{0.6}Bi_2$, and $(La_{0.5}Nd_{0.5})Zn_{0.6}Bi_2$ was performed through EDX using a Phenom Pro Desktop SEM and Phenom ProSuite Software.

X-ray photoelectron spectroscopy (XPS): The XPS testing was carried out in the instrument ThermoFisher NEXSA model using Al Kα monochromatic, X-ray source with an analysis area of 400µm. The system is maintained on specification using Cu, Au, and Ag for regular calibration. A regular calibration check of Ag $3d_{5/2}$ at 386.2eV is verified before experiments. The sample was sputtered using Ar gas using monatomic sputtering to remove any oxygen and carbon contamination from the surface. The pass energy of 50 eV, analyzer resolution of 0.1eV, and the number of scans at 10 were set as parameters.

Calculations: Two model structures, $NdZn_{0.5}Bi_2$ and $NdZnBi_2$, were used in first-principle calculations. They are both from the experimental structure determined from XRD. $NdZnBi_2$ ignored the partial occupancy of Zn and assigned full occupancy. $NdZn_{0.5}Bi_2$ was built by removing one of the two Zn sites in the unit cell, which reduced the symmetry from *P*4/*nmm* to *P*-4*m*2, to simulate the experimental 0.56 Zn occupancy. Vienna Ab-initio Simulation Package [73-76] was used for the calculations. The Perdew−Burke−Ernzerhof (PBE) functional within the generalized gradient approximation (GGA) [77] was adopted to calculate the exchange-correlation potential. The Brillouin zone was sampled using a Monkhorst−Pack *k*-point mesh of 5 × 5 × 9 [78]. Pseudopotentials generated with the projector augmented-wave (PAW) method were employed [79]. To treat the highly correlated Nd 4*f* electrons, spin polarization and the on-site repulsion Hubbard parameter, U = 5 eV, were employed [80].

Physical properties. Electronic transport measurements were performed using a standard 4-probe method in a Quantum Design Physical Property Measurement System (PPMS). Magnetization measurements were carried out using a Quantum Design Magnetic Property Measurement System (MPMS3 SQUID).

Results and Discussions

Crystal Structure

$NdZn_{0.6}Bi_2$, $(La_{0.5}Pr_{0.5})Zn_{0.6}Bi_2$, and $(La_{0.5}Nd_{0.5})Zn_{0.6}Bi_2$ are isostructural and belong to the RE-T-Pn_2 (RE=La-Lu, T=Mn, Fe, Co, Ni, Zn; Pn=P, As, Sb, Bi) family [44-70]. The RE-T-Pn_2 family has been extensively studied back to 1983 in the research of $RNiSb_2$ (R=Ce, Pr, Nd, Sm) [59,63,64,69]. In recent years, exotic physical properties such as the Dirac fermions were found within materials that host square pnictogens layers [44,51,81-86], which reignite the research interest of the RE-T-Pn_2 family. In this work, we reported three bismuth-based materials. To simplify the discussion, $NdZn_{0.6}Bi_2$ is selected as an example to present the crystal structure.

$NdZn_{0.6}Bi_2$ crystallizes in the tetragonal space group *P*4/*nmm* (no. 119) with unit cell parameters of a = 4.53190(14) Å, c = 9.7060(6) Å and a unit cell volume of 199.343(17) $Å^3$. $NdZn_{0.6}Bi_2$ crystallizes in the $HfCuSi_2$ structure type. The crystal structure of $NdZn_{0.6}Bi_2$ is shown in **Figure 1**. $NdZn_{1-x}Bi_2$ is constructed by [Bi] square nets and [$Zn_{1-x}Bi$] layers that sandwich the Nd cations. The Nd atoms are surrounded by eight Bi atoms within the bond distance range of 3.3156(11)-3.389(2) Å, which are comparable to $(La_{0.5}Pr_{0.5})Zn_{0.6}Bi_2$ (3.3424(5)- 3.4222(11) Å),

$(La_{0.5}Nd_{0.5})Zn_{0.6}Bi_2$ (3.3398(3)- 3.4183(6) Å) and many other bismuthides such as NdPdBi (3.389 Å) [87], $Ca_{3.33}Nd_{0.67}Bi_3$ (3.210-3.448 Å) [88], $Nd_3Au_3Bi_4$ (3.484-3.571 Å) [89], $NdNi_{0.64}Bi_2$ (3.310-3.420 Å) [90], $NdNi_2Bi_2$ (3.351-3.584 Å) [91], Nd_3MnBi_5 (3.223-3.447 Å) [92], Nd_5CuBi_3 (3.222-3.478 Å) [93], etc. The $[Zn_{1-x}Bi]$ layers are constructed by $[ZnBi_4]$ tetrahedra. The Zn-Bi bond length is 2.7074(14) Å, which is comparable to that of $(La_{0.5}Pr_{0.5})Zn_{0.6}Bi_2$ (2.7410(7) Å) and $(La_{0.5}Nd_{0.5})Zn_{0.6}Bi_2$ (2.7379(4) Å). There are two independent bismuth atoms in $NdZn_{0.6}Bi_2$. One is linked to Zn and Nd atoms. Another independent bismuth atom is connected to four neighboring bismuth atoms to form the [Bi] square net (**Figure 1b**). The Bi-Bi distance is 3.20454(10) Å, which agrees well with many known compounds with homoatomic Bi-Bi bonds such as $(La_{0.5}Pr_{0.5})Zn_{0.6}Bi_2$ (3.22695(15)Å), $(La_{0.5}Nd_{0.5})Zn_{0.6}Bi_2$ (3.22554(15) Å), $NdNi_{0.64}Bi_2$(3.200 Å) [90], $NdNi_2Bi_2$(3.197 Å) [91], Nd_3MnBi_5(3.204Å) [92], and LiBi(3.361 Å) [94].

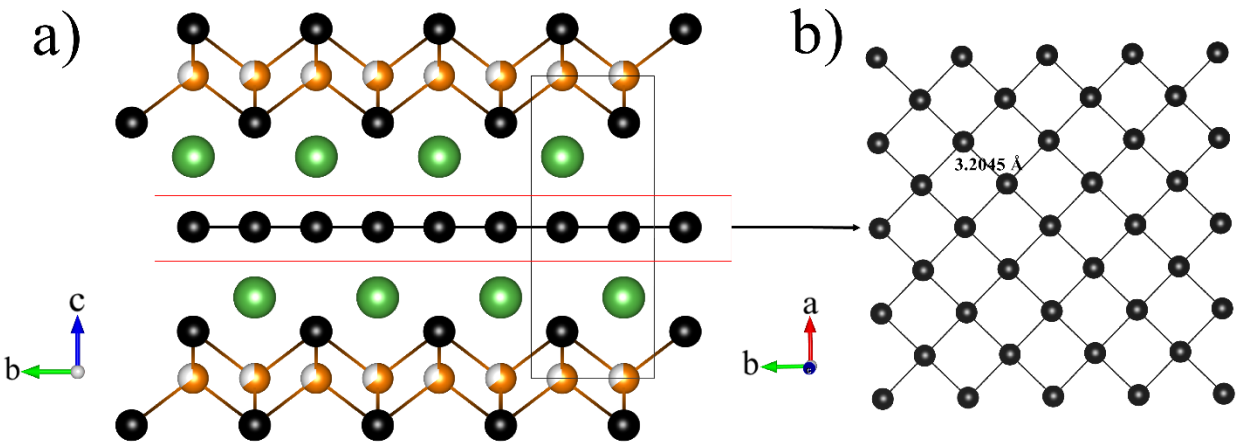

Figure 1. (a) Crystal structure of $NdZn_{0.6}Bi_2$ with unit cell outlined, (b) the square net layer of Bi with Bi-Bi bond distance labeled. Nd: green, Zn: orange, Bi: black.

Applying Zintl-Klemm rules to count electrons reveals the importance of the Zn content and oxidation state in $NdZn_{0.6}Bi_2$. The Bi atoms within the [Bi] square nets are assigned as 1^- due to their four-coordination nature, while Bi atoms within $[Zn_{1-x}Bi]$ layers are assigned as 3^- [23]. Nd and Zn are assigned as 3^+ and 2^+, respectively. Therefore, $NdZn_{0.6}Bi_2$, $[Nd]^{3+}[Zn_{0.6}]^{2+}[Bi]^{3-}[Bi]^{1-}$ should be an electron-rich metal, which was confirmed by transport property measurements (*vide infra*). Based on the above analysis, the charge-balanced formula should be $NdZn_{0.5}Bi_2$ ($[Nd]^{3+}[Zn_{0.5}]^{2+}[Bi]^{3-}[Bi]^{1-}$), which however was not observed in our experiments. This leaves a

natural question of what are the actual oxidation states of constituent elements within $NdZn_{0.6}Bi_2$. A previous study on $CeNi_{0.8-x}Mn_xBi_2$ has revealed the existence of Ni^{2+}/Ni^{3+} and Mn^{2+}/Mn^{3+} [49]. To clarify the oxidation state, we employed XPS of constituent elements in $NdZn_{0.6}Bi_2$.

XPS

The XPS spectrum of Nd-3d and Bi-4f are shown in **Figures** S2 and S3, respectively. The major binding energy (BE) peaks of the Nd-3d are 981.56 eV and 1004.09 eV, which can be assigned as Nd^{3+} [95-99]. The trivalent nature of Nd within $NdZn_{0.6}Bi_2$ was also verified by magnetic property measurements (*vide infra*). Four BE peaks were detected for Bi-4f for $NdZn_{0.6}Bi_2$ (155.91 eV, 161.23 eV, 157.9 eV, 163.21 eV). The two BE peaks of 157.9 eV and 163.21 eV originated from surface Bi_2O_3, which can be removed by heave etch (**Figure** S4). The presence of both Bi^{3-} and Bi^{1-} promoted us synthesizing NdBi [100] and LiBi [94] as reference materials. As shown in **Figures** S5 and S6, the BE of Bi-4f within NdBi and LiBi are comparable with Bi-4f of $NdZn_{0.6}Bi_2$. It seems that the XPS peaks of Bi^{3-} and Bi^{1-} overlap with each other within $NdZn_{0.6}Bi_2$.

Electronic Structure

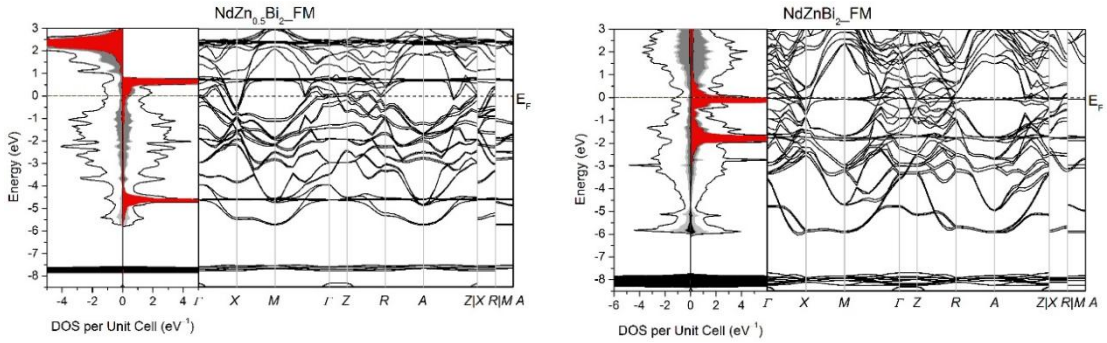

Figure 2. The total and partial DOS and electronic band structure of $NdZn_{0.5}Bi_2$ (left) and $NdZnBi_2$ (right). The black DOS curves are the total DOS for majority and minority spins. The total DOS is projected to the partial DOS to show the contribution by Nd-4*f* (red); Nd-5*d*&6*s* (dark gray); Zn-3*d* (dark); Zn-4*s*&4*p* (light gray); and Bi-6*s*&6*p* (white).

To study the electronic structures of $NdZn_{1-x}Bi_2$, we calculated the DOS and electronic band structures for two model structures, $NdZn_{0.5}Bi_2$ and $NdZnBi_2$. The computational details are in the Experimental section above. The electronic structures of $NdZn_{0.5}Bi_2$ are shown in **Figure 2** left. The Fermi level is located in a state-deficient region (pseudo-gap), indicating a weak metallic nature of $NdZn_{0.5}Bi_2$. Electrical property measurements verified the metallic nature of the

experimental phase, $NdZn_{0.6}Bi_2$ (*vide infra*). The states around the Fermi level are dominantly from Bi so the metallicity originates from the Bi square nets. The Fermi level in a pseudo-gap usually signifies electron-balancing. This is indeed the case for the composition of $NdZn_{0.5}Bi_2$ if we simplistically count the valences as $[Nd]^{3+}[Zn_{0.5}]^{2+}[Bi]^{3-}[Bi]^{1-}$.

Increasing the Zn content from $NdZn_{0.5}Bi_2$ to $NdZnBi_2$ makes the phase electron-rich if we simplistically assign the valences as $[Nd]^{3+}[Zn]^{2+}[Bi]^{3-}[Bi]^{1-}$, where Nd and Zn donate 5 electrons while Bi accommodates 4 only. This is shown in the electronic structure of $NdZnBi_2$ that the Fermi level is lifted ~0.5 eV above the pseudogap (**Figure 2**, right). Moreover, Nd-4f states dominates the states around the Fermi level, indicating that, instead of Bi or Zn, the extra electrons mainly populate Nd-4f states. This is not physically possible as Nd is the most electropositive element among the three elements of Nd, Zn, and Bi.

The experimental composition, $NdZn_{0.6}Bi_2$, was grown by Zn-Bi flux and thus represents the Zn-rich limit for samples obtained by flux methods. It is only slightly different from the first model structure $NdZn_{0.5}Bi_2$. This indicates that the title phase, $NdZn_{1-x}Bi_2$, is not a very strict valence compound. The optimum composition is $NdZn_{0.5}Bi_2$, which is electron exact. However, it can accommodate more Zn and be electron-rich but only to a small extent by flux methods.

Magnetic Properties

The RE-T-Pn_2 family is highly tunable due to structural flexibility. For $NdZn_{0.6}Bi_2$, the rare earth metal (Nd), the 3*d* transition metal (Zn), and the Bi square-net, all can be substituted by other elements. Nd generates magnetism which can be replaced by non-magnetic (such as La) and magnetic rare earth with different *f*-electron numbers. Zn not only contributes electrons which is tunable by occupancy as discussed above, but also can be substituted by other 3*d* metals including magnetic ones like Mn [101-102]. The Bi square-net generates Dirac state which is tunable by spin-orbital coupling and symmetry (like lattice distortion) [101,103]. Such high chemical flexibility results in tunable physical properties, which has been demonstrated in our recent nonlinear optical materials studies [104-112]. Previous work on the RE-T-Pn_2 family has been focused on tuning transition metal contents such as $LaMn_{1-x}Sb_2$ [48] or mixing transition metals such as $CeNi_{0.8-x}Mn_xBi_2$ [49]. Modifying the rare earth layers, however, is relatively less explored. This motivates us to extend the study to two mixed-cation compounds of $(La_{0.5}Pr_{0.5})Zn_{0.6}Bi_2$ and $(La_{0.5}Nd_{0.5})Zn_{0.6}Bi_2$.

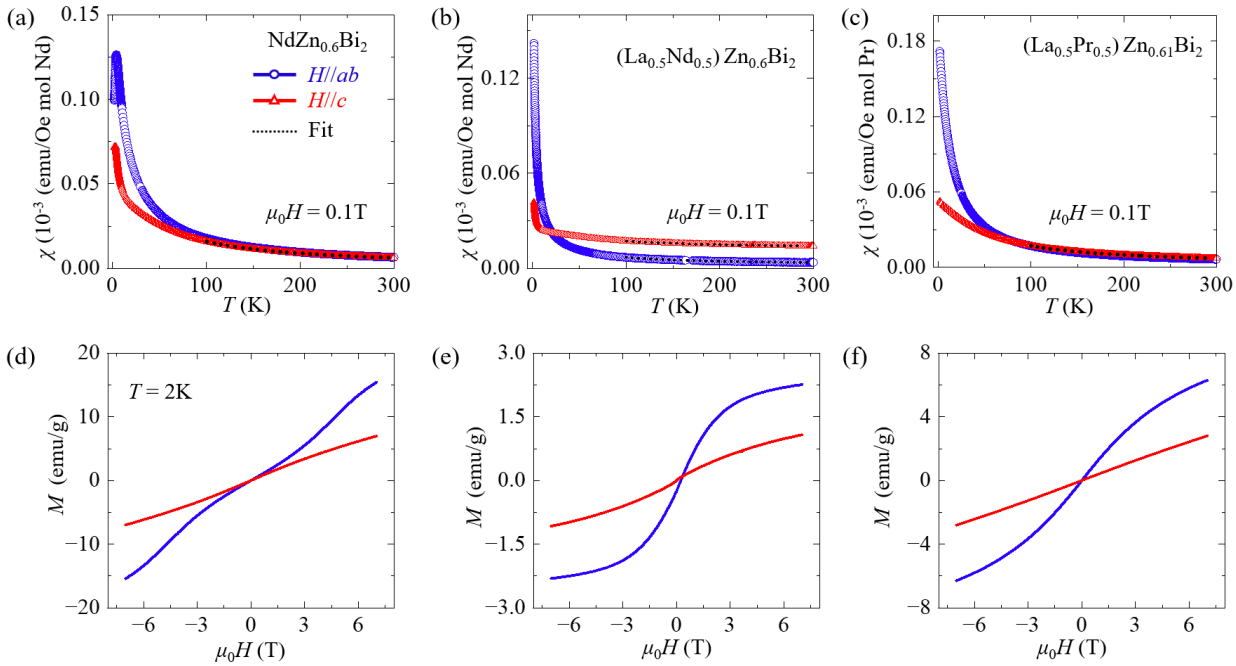

Figure 3. (a, b, c) Temperature dependence of dc magnetic susceptibility (χ) measured under a field of 1000 Oe applied within (*H*//*ab*) and perpendicular (*H*//c) to the *ab* plane for (a) $NdZn_{0.6}Bi_2$, (b) $(La_{0.5}Nd_{0.5})Zn_{0.6}Bi_2$, and (c) $(La_{0.5}Pr_{0.5})Zn_{0.6}Bi_2$. Only zero-field-cooling data is shown because zero-field-cooling and field-cooling data overlaps perfectly (see supplementary **Figures** S7, S9, and S11). The dotted lines in each panel is the fitting to the Curie-Weiss law. (d, e, f) Field dependence of magnetization (*M*) at 2 K measured with magnetic field within (*H*//*ab*) and perpendicular (*H*//*c*) to the *ab* plane for (d) $NdZn_{0.6}Bi_2$, (e) $(La_{0.5}Nd_{0.5})Zn_{0.6}Bi_2$, and (f) $(La_{0.5}Pr_{0.5})Zn_{0.6}Bi_2$. Isothermal magnetization data at various temperatures up to 300 K are provided in Figures S8, S10, and S12.

Table 2. Fitting parameters for $NdZn_{0.6}Bi_2$, $(La_{0.5}Nd_{0.5})Zn_{0.6}Bi_2$, and $(La_{0.5}Pr_{0.5})Zn_{0.6}Bi_2$ obtained from the modified Curie-Weiss fits, from which the effective moment for each sample is obtained. The average moment is obtained by $(2\mu_{ab}+\mu_c)/3$, where μ_{ab} and μ_c are effective moments obtained from in-plane (*H*//*ab*) and out-of-plane (*H*//*c*) susceptibility.

Compound	Field	χ_0 (emu Oe^{-1} per mol RE)	C (emu Oe^{-1} K per mol RE)	Θ_p (K)	μ_{eff} (μ_B per RE)	Average μ_{eff} (μ_B)
$NdZn_{0.6}Bi_2$	*H*//*ab*	0.0000496	2.029	-13.474	4.03	3.98

	$H \perp ab$	0.0003430	1.890	-21.238	3.89	
$(La_{0.5}Nd_{0.5})Zn_{0.6}Bi_2$	$H//ab$	0.001944	0.534	-7.514	2.07	2.25
	$H \perp ab$	0.0116	0.866	-54.918	2.63	
$(La_{0.5}Pr_{0.5})Zn_{0.6}Bi_2$	$H//ab$	0.0104	1.622	-1.144	3.60	3.74
	$H \perp ab$	0.000884	2.062	-26.649	4.06	

The magnetic susceptibility ($\chi = M/H$) of each of $NdZn_{0.6}Bi_2$, $(La_{0.5}Nd_{0.5})Zn_{0.6}Bi_2$, and $(La_{0.5}Pr_{0.5})Zn_{0.6}Bi_2$ was measured on a large plate-like single crystal under a magnetic field of 1000 Oe as shown in **Figures 3a-3c**. Due to the plate-like single crystals with *ab*-plane as a cleavage plane, both in-plane and out-of-plane susceptibilities were measured with in-plane ($H//ab$) and out-of-plane ($H//c$) magnetic field configurations, respectively (**Figures S7-S12**). As shown in **Figure 3a**, $NdZn_{0.6}Bi_2$ exhibits a sharp transition around 3 K, which should correspond to an antiferromagnetic transition owing to the lack of irreversibility between zero-field-cooling (ZFC) and field-cooling (FC) data. In the paramagnetic state, at temperatures well above the transition temperature, magnetic susceptibility can be well-described by the modified Curie-Weiss law $\chi = \chi_0 + C/(T - \Theta_p)$, where χ_0 is a temperature-independent constant, C is the Curie constant, T is the absolute temperature, and Θ_p is the paramagnetic Weiss temperature. The extracted fitting parameters are summarized in **Table 2**. The negative Weiss temperature also implies predominate antiferromagnetic correlations in $NdZn_{0.6}Bi_2$. The effective magnetic moment of 3.98 μ_B per Nd^{3+} is close to the theoretical value of 3.62 μ_B for Nd^{3+}. The trivalent nature of Nd is further confirmed by XPS analysis as indicated above. The magnetism in $NdZn_{0.6}Bi_2$ can be tuned by a magnetic field. As shown in **Figure S7**, the antiferromagnetic transition is suppressed to a lower temperature at the higher magnetic field. Such field-modulation of magnetism is also manifested in the isothermal magnetization measurements. As shown in **Figure 3d**, at $T = 2$ K, a magnetization upturn occurs near 3 T for $H//ab$. Such super-linear field dependence is reminiscent of a spin-flop transition, but the broad magnetization upturn is distinct from a conventional spin-flop transition characterized by abrupt magnetization jump. Therefore, the magnetic moment orientation might be re-oriented in a more gradual way as compared to a spin-flop transition. Furthermore, at low fields near zero field, the linear field dependence for magnetization again supports an antiferromagnetic ground state.

The magnetization measurements under the out-of-plane field (*H*//*c*) reveal anisotropic magnetism. First of all, unlike the sharp magnetic transition seen with the in-plane field, the temperature-dependent magnetic susceptibility (**Figure S9**) does not display a well-defined susceptibility peak. In addition, the field-dependent magnetization under *H*//*c* is also featureless, showing linear dependence up to 7 T, as shown in **Figure 3d**. These observations suggest that the magnetic easy axis might be within the *ab*-plane.

Since magnetism in $NdZn_{0.6}Bi_2$ derives from the Nd 4*f* electrons, it is expected to be tunable by substituting Nd. Indeed, diluting magnetism by substituting non-magnetic La suppresses magnetism. Though a similar susceptibility upturn is seen at low temperatures, $(La_{0.5}Nd_{0.5})Zn_{0.6}Bi_2$ displays no clear magnetic transition down to 2 K for both magnetic field orientations *H*//*ab* (**Figure 3b**) and *H*//*c* (**Figure S11**). The effective moment obtained from the Curie-Weiss fit is 2.25 μ_B per Nd^{3+}, which is smaller than the theoretical value (3.62 μ_B/Nd^{3+}). The reduced effective moment has been proposed to be associated with various mechanisms such as crystal field effect that split the energy levels, spin-orbit coupling that mixes spin and orbital angular momentum and partially quench the magnetic moment, and hybridization of 4f electrons with conduction electrons. In addition, the isothermal field-dependent magnetization at 2 K is strongly modified: under in-plane field *H*//*ab*, magnetization displays a tendency toward saturation, suggesting possible ferromagnetic correlations at higher fields that might be due to magnetic moment canting. Replacing Nd by Pr, i.e., $(La_{0.5}Pr_{0.5})Zn_{0.6}Bi_2$, similar field-dependent magnetization absence of well-defined magnetic transition are observed, as shown in **Figures 3c**, and **3f.** The effective moment obtained from the Curie-Weiss fit is 3.74 μ_B per Pr^{3+}, which is close to the theoretical value of 3.58 μ_B for Pr^{3+}. In addition, the uncertainty in composition determination in this substituted compound, especially the content of Pr, would also result in some errors in calculating effective per rare earth ion. To fully understand it, further theoretical and experimental (such as neutron scattering) would be helpful.

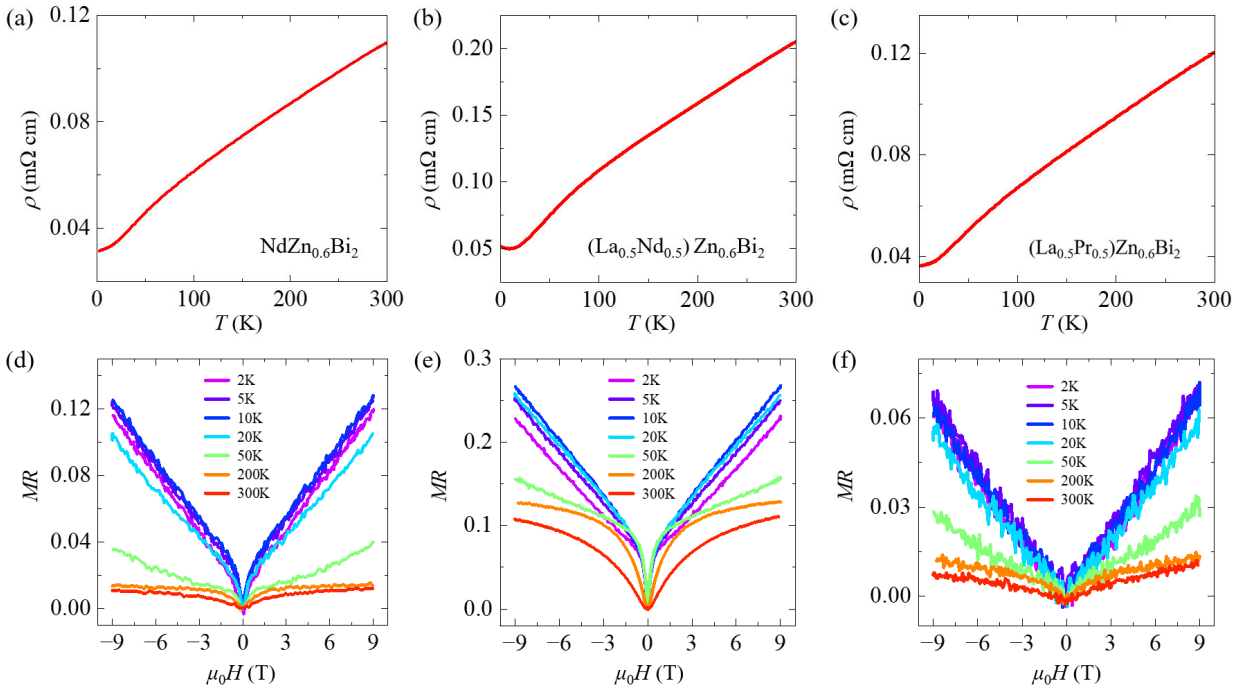

Figure 4. (a, b, c) Temperature dependence of resistivity measured at zero magnetic field for (a) $NdZn_{0.6}Bi_2$, (b) $(La_{0.5}Nd_{0.5})Zn_{0.6}Bi_2$, and (c) $(La_{0.5}Pr_{0.5})Zn_{0.6}Bi_2$. (d, e, f) Magnetoresistance (MR) normalized to the zero-field resistivity value at different temperatures for (d) $NdZn_{0.6}Bi_2$, (e) $(La_{0.5}Nd_{0.5})Zn_{0.6}Bi_2$, and (f) $(La_{0.5}Pr_{0.5})Zn_{0.6}Bi_2$.

Figure 4 shows the electrical transport properties of the three compounds. As shown in Figures **4a-4c**, all samples exhibit metallic character with decreasing resistivity up on cooling, which is consistent with the electronic band structure calculations as stated above. At 300 K, $NdZn_{0.6}Bi_2$, $(La_{0.5}Nd_{0.5})Zn_{0.60}Bi_2$, and $(La_{0.5}Pr_{0.5})Zn_{0.61}Bi_2$ possess comparable resistivity values within 0.11 – 0.21 mΩ cm. The variations between samples might be attributed to the property variation or some uncertainty in estimating the sample dimensions for converting resistivity. Compared to the absolute resistivity values, the residual resistivity ratio (RRR), defined as the ratio of the resistivities at 300 K and 2 K, rules out uncertainties in sample dimension measurements and hence better reflects the evolution of the electronic properties. RRR is 3.4, 4.1, and 3.3 for $NdZn_{0.6}Bi_2$, $(La_{0.5}Nd_{0.5})Zn_{0.60}Bi_2$, and $(La_{0.5}Pr_{0.5})Zn_{0.61}Bi_2$, respectively, indicating that these compounds are not good metals.

Upon applying magnetic fields, all compounds display positive magnetoresistance (MR) characterized by increased resistivity. The normalized MR, defined as resistivity change

normalized to the zero-field value MR = [$\rho(H)$- $\rho(H$=0T)]/$\rho(H$=0T), reaches ~12% at 2 K and 9 T for $NdZn_{0.6}Bi_2$, as shown in **Figure 4d**. MR is enhanced to ~25% in $(La_{0.5}Nd_{0.5})Zn_{0.6}Bi_2$ (**Figure 4e**), while reduced to ~6% in $(La_{0.5}Pr_{0.5})Zn_{0.6}Bi_2$ (**Figure 4f**). Rather than a quadric field dependence expected for orbital MR in simple metals, here MR in all three compounds display a clear dip at zero field, which is reminiscent of weak antilocalization and suggests the involvement of quantum effect in electronic properties. Weak antilocalization originates from quantum interference of time-reversal symmetric backscattering electron trajectories. The interference is destructive in the presence of strong spin-orbital coupling, which suppresses backscattering rate and consequently the resistance. The suppression of such interference by magnetic field effectively enhances the resistance, leading to an MR dip near zero field. Such weak antilocalization effect appears to be the strongest in $(La_{0.5}Nd_{0.5})Zn_{0.6}Bi_2$ while the weakest in $(La_{0.5}Pr_{0.5})Zn_{0.61}Bi_2$. Considering that MR is also strong in $(La_{0.5}Nd_{0.5})Zn_{0.6}Bi_2$ while weak in $(La_{0.5}Pr_{0.5})Zn_{0.61}Bi_2$, weak antilocalization might dominate the MR behavior.

Conclusions

Three new bismuthides, $NdZn_{0.6}Bi_2$, $(La_{0.5}Nd_{0.5})Zn_{0.6}Bi_2$, and $(La_{0.5}Pr_{0.5})Zn_{0.6}Bi_2$ were grown as millimeter-sized crystals by Zn-Bi flux. Structure studies revealed that these new bismuthides crystallize in the $HfCuSi_2$ structure type and belong to the RE-T-Pn_2 (RE=La-Lu, T=Mn, Fe, Co, Ni, Zn; Pn=P, As, Sb, Bi) material family. The existence of vacancies at the Zn site made experimental $NdZn_{0.6}Bi_2$ an electron-rich composition according to the Zintl principles. The importance of Zn contents was verified by DFT calculation. Varying Zn contents can form both electron-balanced composition $NdZn_{0.5}Bi_2$ and electron-rich composition $NdZnBi_2$. XPS was employed to study the oxidation states of constituent elements of $NdZn_{0.5}Bi_2$. There are two binding energy peaks of 155.91 eV and 161.23 eV detected for Bi atoms within $NdZn_{0.6}Bi_2$. NdBi and LiBi were synthesized as reference materials. The binding energy peaks of Bi within NdBi and LiBi are very similar to $NdZn_{0.6}Bi_2$. The two oxidation states of Bi^{3-} and Bi^{-} cannot be distinguished by XPS. The trivalent nature of Nd was further confirmed by magnetic measurements. Furthermore, magnetic measurements reveal an antiferromagnetic ground state for $NdZn_{0.5}Bi_2$ below 3 K with an in-plane magnetic easy axis, whereas La and Pr substitutions can suppress magnetic ordering temperature. $NdZn_{0.6}Bi_2$ possesses a small magnetoresistance of 12% at 2K with a magnetic field of 9T. $(La_{0.5}Pr_{0.5})Zn_{0.6}Bi_2$ show reduced magnetoresistance compared

with $NdZn_{0.6}Bi_2$ under identical conditions (6%). $(La_{0.5}Nd_{0.5})Zn_{0.6}Bi_2$ possesses enhanced magnetoresistance of 25% at 2K with a magnetic field of 9T.

ASSOCIATED CONTENT

Supporting Information

The powder X-ray diffraction patterns, EDS results, refined crystallographic data, XPS results, and magnetic properties. (DOC)

Acknowledgments

This research was supported by the U.S. National Science Foundation under grant OSI-2328822. J.H. acknowledges the support from NSF Career Award under Grant No. DMR-2238254.

Corresponding author:

Jin Hu jinhu@uark.edu

Jian Wang jian.wang@wichita.edu

Notes

The authors declare no competing financial interest.

References

1. Kauzlarich, S. M. Zintl Phases: From Curiosities to Impactful Materials. *Chem. Mater.* **2023**, *35* (18), 7355–7362.https://doi.org/10.1021/acs.chemmater.3c01874.

2. Schäfer, H.; Eisenmann, B.; Müller, W. Zintl Phases: Transitions between Metallic and Ionic Bonding. *Angew. Chem., Int. Ed.* **1973**, *12*(9),694−712.https://doi.org/10.1002/anie.197306941.

3. Schäfer, H. On the Problem of Polar Intermetallic Compounds: The Stimulation of E. Zintl's Work for the Modern Chemistry of Intermetallics. *Annu. Rev. Mater. Sci.* **1985**, *15* (1), 1–42.https://doi.org/10.1146/annurev.ms.15.080185.000245.

4. Schäfer, H. Semimetal Clustering in Intermetallic Phases. *J. Solid State Chem.* **1985**, *57* (1), 97–111. https://doi.org/10.1016/s0022-4596(85)80063-3.

5. Kauzlarich, S. M. A rational approach to solid state synthesis-the Zintl concept. *Comment Inorg. Chem.* **1990**, *10* (2−3), 75−88. https://doi.org/10.1080/02603599008050859.

6. Kauzlarich, S. M. *Chemistry, Structure, and Bonding of Zintl Phases and Ions*; VCH Publishers, Inc.: New York, 1996.

7. Kauzlarich, S. M.; Kuromoto, T. Y.; Olmstead, M. M. Preparation and Structure of a New Ternary Transition Metal Zintl Compound Containing High Spin Manganese-Bismuth MnIIIBi$_4$ Tetrahedra. *J. Am. Chem. Soc.* **1989**, *111* (20), 8041–8042.https://doi.org/10.1021/ja00202a069.

8. Kauzlarich, S. M. Transition Metal Zintl Compounds. *In Chemistry, Structure, and Bonding of Zintl Phases and Ions*, Kauzlarich,S. M., Ed.; VCH Publishers, Inc., 1996; pp 245−274.

9. Kauzlarich, S. M.; Payne, A. C.; Webb, D. J. Magnetism andMagnetotransport Properties of Transition Metal Zintl Isotypes. In *Magnetism: Molecules to Materials III*; Miller, J. S., Drillon, M., Eds.;Wiley-VCH, 2002; pp 37−62.

10. Brown, S. R.; Kauzlarich, S. M.; Gascoin, F.; Snyder, G. J. Yb$_{14}$MnSb$_{11}$: New High Efficiency Thermoelectric Material for Power Generation. *Chem. Mater.* **2006**, *18* (7), 1873–1877.https://doi.org/10.1021/cm060261t

11. Kauzlarich, S. M.; Brown, S. R.; Jeffrey Snyder, G. Zintl phases for thermoelectric devices. *Dalton Trans*. **2007**, No. 21, 2099−2107.https://doi.org/10.1039/b702266b.

12. Wang, J.; Yang, M.; Pan, M.-Y.; Xia, S.-Q.; Tao, X.-T.; He, H.; Darone, G.; Bobev, S. Synthesis, Crystal and Electronic Structures, and Properties of the New Pnictide Semiconductors A_2CdPn_2 (A = ca, Sr, Ba, Eu; Pn = P, As). *Inorg. Chem.* **2011**, *50* (17), 8020–8027.https://doi.org/10.1021/ic200286t.

13. Wang, J.; Xia, S.-Q.; Tao, X.-T. A$_5$Sn$_2$As$_6$ (A = Sr, Eu). Synthesis, Crystal and Electronic Structure, and Thermoelectric Properties. *Inorg. Chem.* **2012**, *51* (10), 5771–5778.https://doi.org/10.1021/ic300308w.

14. Wang, J.; Xia, S.-Q.; Tao, X.-T. Syntheses, Crystal Structure and Physical Properties of New Zintl Phases Ba$_3$T$_2$As$_4$ (T=Zn, Cd). *J. Solid State Chem.* **2013**, *198*, 6-9. https://doi.org/10.1016/j.jssc.2012.09.029.

15. Wang, J.; Xia, S.-Q.; Tao, X.-T.; Schäfer, M. C.; Bobev, S. New Ternary Phosphides and Arsenides. Syntheses, Crystal Structures, Physical Properties of Eu$_2$ZnP$_2$, Eu$_2$Zn$_2$P$_3$ and Eu$_2$Cd$_2$As$_3$. *J. Solid State Chem.* **2013**, *205*, 116–121.https://doi.org/10.1016/j.jssc.2013.06.029.

16. Liu, X.-C.; Lin, N.; Wang, J.; Pan, M.-Y.; Zhao, X.; Tao, X.-T.; Xia, S.-Q. $Ba_{13}Si_6Sn_8As_{22}$: A Quaternary Zintl Phase Containing Adamantane-like [Si_4As_{10}] Clusters. *Inorg. Chem.* **2013**, *52* (20), 11836–11842.https://doi.org/10.1021/ic402023z.

17. Wang, J.; Xia, S.-Q.; Tao, X.-T. $A_{10}LaCdSb_9$ (A=Ca, Yb): A Highly Complex Zintl System and the Thermoelectric Properties. *Chem. Asian J.* **2013**, *8* (1), 251–257.https://doi.org/10.1002/asia.201200827.

18. Wang, J.; Liu, X.-C.; Xia, S.-Q.; Tao, X.-T. $Ca_{1-x}RE_xAg_{1-y}Sb$ (RE = La, Ce, Pr, Nd, Sm; $0 \leq x \leq 1$; $0 \leq y \leq 1$): Interesting Structural Transformation and Enhanced High-Temperature Thermoelectric Performance. *J. Am. Chem. Soc.* **2013**, *135* (32), 11840–11848.10.1021/ja403653m.

19. Eickmeier, K.; Steinberg, S. Exploring the Frontier between Polar Intermetallics and Zintl Phases for the Examples of the Prolific $ALnTnTe_3$-Type Alkali Metal (A) Lanthanide (Ln) Late Transition Metal (Tn) Tellurides. *Z. Naturforsch. B J. Chem. Sci.* **2021**, *76* (10–12), 635–642. https://doi.org/10.1515/znb-2021-0100.

20. Guloy, A. M. Polar Intermetallics and Zintl Phases along the Zintl Border. *Inorganic Chemistry in Focus III*. Wiley July 20, 2006, pp 157–171. https://doi.org/10.1002/9783527609932.ch10.

21. Göbgen, K. C.; Gladisch, F. C.; Steinberg, S. The Mineral Stützite: A Zintl-Phase or Polar Intermetallic? A Case Study Using Experimental and Quantum-Chemical Techniques. *Inorg. Chem.* **2018**, *57* (1), 412–421. https://doi.org/10.1021/acs.inorgchem.7b02642.

22. Gladisch, F. C.; van Leusen, J.; Passia, M. T.; Kögerler, P.; Steinberg, S. $Rb_3Er_4Cu_5Te_{10}$: Exploring the Frontier between Polar Intermetallics and Zintl-phases via Experimental and Quantumchemical Approaches. *Eur. J. Inorg.Chem.***2021**,*2021*(47),4946–4953. https://doi.org/10.1002/ejic.202100795.

23. Papoian, G. A.; Hoffmann, R. Hypervalent Bonding in One, Two, and Three Dimensions: Extending the Zintl-Klemm Concept to Nonclassical Electron-Rich Networks. *Angew. Chem., Int. Ed. Engl.* **2000**, *39* (14), 2408–2448.DOI:10.1002/1521-3773(20000717)39:14<2408::aid-anie2408>3.0.co;2-u.

24. Nesper, R. Structure and Chemical bonding in Zintl-phases containing Li. *Prog. Sol. State Chem*. **1990**, *20*, 1−45.https://doi.org/10.1016/0079-6786(90)90006-2.

25. Miller, G. J.; Schmidt, M. W.; Wang, F.; You, T.-S. Quantitative Advances in the Zintl-Klemm Formalism. *In Zintl Phases: Principles and Recent Developments*; Fassler, T. F., Ed.; Structure and Bonding, Vol.139; Springer-Verlag, 2011; pp 1−55.

26. Nesper, R. The Zintl-Klemm Concept - A Historical Survey. *Z.Anorg. Allg. Chem*. **2014**, *640* (14), 2639−2648. https://doi.org/10.1002/zaac.201400403.

27. Hu, Y.; Cerretti, G.; Kunz Wille, E. L.; Bux, S. K.; Kauzlarich, S. M. The Remarkable Crystal Chemistry of the $Ca_{14}AlSb_{11}$ Structure Type, Magnetic and Thermoelectric Properties. *J. Solid State Chem.* **2019**, *271*, 88–102.https://doi.org/10.1016/j.jssc.2018.12.037

28. Ogunbunmi, M. O.; Bobev, S. Exploiting the fraternal twin nature of thermoelectrics and topological insulators in Zintl phases as a tool for engineering new efficient thermoelectric generators. *J. Mater. Chem. C,* **2023**, *11* (25), 8337−8357.https://doi.org/10.1039/d3tc00556a.

29. Toberer, E. S.; May, A. F.; Snyder, G. J. Zintl Chemistry for Designing High Efficiency Thermoelectric Materials. *Chem. Mater.* **2010**, *22* (3), 624–634.https://doi.org/10.1021/cm901956r

30. Liu, K.-F.; Xia, S.-Q. Recent progresses on thermoelectric Zintl phases: Structures, materials and optimization. *J. Solid State Chem*. **2019**, *270*, 252−264.https://doi.org/10.1016/j.jssc.2018.11.030

31. Ovchinnikov, A.; Bobev, S. Zintl phases with group 15 elements and the transition metals: A brief overview of pnictides with diverse andcomplex structures. *J. Solid State Chem*. **2019**, *270*, 346−359.https://doi.org/10.1016/j.jssc.2018.11.029

32. Fässler, T. F. *Zintl Ions: Principles and Recent Developments*;Springer-Verlag: Berlin, Heidelberg, 2011.

33. Cameron, J. M.; Hughes, R. W.; Zhao, Y.; Gregory, D. H. Ternary and higher pnictides; prospects for new materials and applications.*Chem. Soc. Rev*. **2011**, *40* (7), 4099−4118.https://doi.org/10.1039/c0cs00132e.

34. Kauzlarich, S. M. Special Issue: Advances in Zintl Phases.*Materials (Basel)* , **2019**, *12* (16), 2554.**https://doi.org/10.3390/ma12162554**

35. Fang, S.; Li, J.; Zou, K.; Shuai, H.; Xu, L.; Deng, W.; Zou, G.;Hou, H.; Ji, X. Zintl chemistry: Current status and future perspectives.*Chem. Eng. J.* **2022**, *433*, 133841.https://doi.org/10.1016/j.cej.2021.133841

36. Zhang, J. H.; Van Duyneveldt, A. J.; Mydosh, J. A.; O'Connor, C.J. A New Amorphous Magnetic Material: $Fe_5(InTe_4)_2$. *Chem. Mater*.**1989**, *1*, 404−406.https://doi.org/10.1021/cm00004a005

37. Scharfe, S.; Kraus, F.; Stegmaier, S.; Schier, A.; Fassler, T. F. Zintl ions, cage compounds, and intermetalloid clusters of Group 14 and Group 15 elements. *Angew. Chem., Int. Ed. Engl.* **2011**, *50* (16), 3630−3670.https://doi.org/10.1002/anie.201001630.

38. Bianco, E.; Butler, S.; Jiang, S.; Restrepo, O. D.; Windl, W.;Goldberger, J. E. Stability and Exfoliation of Germanane: A Germanium Graphane Analogue. *ACS Nano*, **2013**, *7* (5), 4414−4421.https://doi.org/10.1021/nn4009406

39. Molle, A.; Goldberger, J.; Houssa, M.; Xu, Y.; Zhang, S. C.;Akinwande, D. Buckled two-dimensional Xene sheets.*Nat.Mater.***2017**,*16*(2), 163−169.https://doi.org/10.1038/nmat4802

40. Beekman, M.; Kauzlarich, S. M.; Doherty, L.; Nolas, G. S. Zintl Phases as Reactive Precursors for Synthesis of Novel Silicon and Germanium-Based Materials. *Materials(Basel)*,**2019**, *12* (7), 1139. https://doi.org/10.3390/ma12071139

41. Shumiya, N.; Hossain, M. S.; Yin, J.-X.; Wang, Z.; Litskevich, M.; Yoon, C.; Li, Y.; Yang, Y.; Jiang, Y.-X.; Cheng, G.; Lin, Y.-C.; Zhang, Q.; Cheng, Z.-J.; Cochran, T. A.; Multer, D.; Yang, X. P.; Casas, B.; Chang, T.-R.; Neupert, T.; Yuan, Z.; Jia, S.; Lin, H.; Yao, N.; Balicas, L.; Zhang, F.; Yao, Y.; Hasan, M. Z. Evidence of a Room-Temperature Quantum Spin Hall Edge State in a Higher-Order Topological Insulator. *Nat. Mater.* **2022**, *21* (10), 1111–1115. https://doi.org/10.1038/s41563-022-01304-3.

42. He, K. $MnBi_2Te_4$-Family Intrinsic Magnetic Topological Materials. *Npj Quantum Mater.* **2020**, *5* (1),90.https://doi.org/10.1038/s41535-020-00291-5

43. Le Mardelé, F.; Wyzula, J.; Mohelsky, I.; Nasrallah, S.; Loh, M.; Ben David, S.; Toledano, O.; Tolj, D.; Novak, M.; Eguchi, G.; Paschen, S.; Barišić, N.; Chen, J.; Kimura, A.; Orlita, M.; Rukelj, Z.; Akrap, A.; Santos-Cottin, D. Evidence for Three-Dimensional Dirac Conical Bands in TlBiSSe by Optical and Magneto-Optical Spectroscopy.*Phys.Rev.B.* **2023**, *107* (24),L241101.https://doi.org/10.1103/physrevb.107.l241101.

44. Shi, X.; Richard, P.; Wang, K.; Liu, M.; Matt, C. E.; Xu, N.; Dhaka, R. S.; Ristic, Z.; Qian, T.; Yang, Y.-F.; Petrovic, C.; Shi, M.; Ding, H. Observation of Dirac-like Band Dispersion in $LaAgSb_2$. *Phys. Rev. B.* **2016**, *93* (8),081105.https://doi.org/10.1103/physrevb.93.081105.

45. Zelinska, O. Ya.; Mar, A. Structure and electrical resistivity of rare-earth zinc bismuthides $REZn_{1-x}Bi_2$ (RE = La, Ce, Pr). *J. Alloys Compd.* **2008**, *451*, 606–609.https://doi.org/10.1016/j.jallcom.2007.04.073

46. Li, Y.; Yang, M.; Yan, S.; Miao, S.; Yang, H.; Feng, H.; Shi, Y. Crystal growth and magnetic properties of $LaMn_{0.91}Sb_2$ and $NdMn_{0.88}Sb_2$. *Phys. Rev. B.* **2022**, *105*, 224429.https://doi.org/10.1103/PhysRevB.105.224429

47. Yang, T.; Zhang, L.; Wang, C.-W.; Gao, F.; Xia, Y.; Jiang, P.; Zhang, L.; Mi, X.; He, M.; Chai, Y.; Zhou, X.; Fu, H.; Re, W.; Wang, A.; Single-crystal growth and physical properties of $LaMn_{0.86}Sb_2$. *Phys. Rev. B.* **2022,** *107***,** 115150.https://doi.org/10.1103/physrevb.107.115150.

48. Slade, T. J.; Sapkota, A.; Wilde, J. M.; Zhang, Q.; Wang, L.-L.; Lapidus, S. H.; Schmidt, J.; Heitmann, T.; Bud'ko, S. L.; Canfield, P. C. Vacancy-Tuned Magnetism in $LaMn_xSb_2$. *Phys. Rev. Mater*. **2023**, *7* (11), 114203.https://doi.org/10.1103/physrevmaterials.7.114203.

49. Kim, S-W.; Lee, K.; Adroja, D. T.; Demmel, F.; Taylor, J. W.; Jung, M-H. Substitution effect on the magnetic and transport properties of $CeNi_{0.8-x}Mn_xBi_2$. *J. Appl. Phys.* **2014**, *116*, 073901.https://doi.org/10.1063/1.4893304

50. Bud'ko, S. L.; Law, S. A.; Canfield, P. C.; Samolyuk, G. D.; Torikachvili, M. S.; Schmiedeshoff, G. M. Thermal Expansion and Magnetostriction of Pure and Doped $RAgSb_{(2)}$ (R = Y, Sm, La) Single Crystals. *J. Phys. Condens. Matter* **2008**, *20* (11), 115210.https://doi.org/10.1088/0953-8984/20/11/115210.

51. Wang, K.; Petrovic, C. Multiband Effects and Possible Dirac States in $LaAgSb_2$. *Phys. Rev. B.* **2012**, *86* (15). 155213.https://doi.org/10.1103/physrevb.86.155213.

52. Mizoguchi, H.; Matsuishi, S.; Hirano, M.; Tachibana, M.; Takayama-Muromachi, E.; Kawaji, H.; Hosono, H. Coexistence of Light and Heavy Carriers Associated with Superconductivity and Antiferromagnetism In $CeNi_{0.8}Bi_2$ with a Bi Square Net. *Phys. Rev. Lett.* **2011**, *106* (5), 057002.https://doi.org/10.1103/physrevlett.106.057002.

53. Wollesen, P.; Jeitschko, W.; Brylak, M.; Dietrich, L. Ternary Antimonides $LnM_{1-x}Sb_2$ with Ln = La, Nd, Sm, Gd, Tb and M = Mn, Co, Au, Zn, Cd. *J. Alloys Compd.* **1996**, *245* (1–2), L5–L8.https://doi.org/10.1016/s0925-8388(96)02391-2

54. Takahashi, Y.; Urata, T.; Ikuta, H. Metamagnetic Transitions Associated with Two Antiferromagnetic Phases of $PrMn_{1-x}Sb_2$ and Its Magnetic Phase Diagram. *Phys. Rev. B.* **2021**, *104* (5), 054408.https://doi.org/10.1103/PhysRevB.104.054408.

55. Leithe-Jasper, A.; Rogl, P. The Crystal Structure of $NdFe_{1-x}Sb_2$ and Isotypic Compounds $RE(Fe, Co)_{1-x}Sb_2$ (RE =La, Ce, Pr, Sm, Gd). *J. Alloys Compd.* **1994**, *203*, 133–136.https://doi.org/10.1016/0925-8388(94)90723-4.

56. Myers, K. D.; Bud'ko, S. L.; Antropov, V. P.; Harmon, B. N.; Canfield, P. C.; Lacerda, A. H. De Haas–van Alphen and Shubnikov–de Haas Oscillations In $RAgSb_2$(R=Y,La-Nd, Sm). *Phys. Rev. B.* **1999**, *60* (19), 13371–13379.https://doi.org/10.1103/physrevb.60.13371.

57. Arakane, T.; Sato, T.; Souma, S.; Takahashi, T.; Watanabe, Y.; Inada, Y. Electronic Structure of $LaAgSb_2$ and $CeAgSb_2$ Studied by High-Resolution Angle-Resolved Photoemission Spectroscopy. *J. Magn. Magn. Mater.* **2007**, *310* (2), 396–398.https://doi.org/10.1016/j.jmmm.2006.10.101.

58. Jesus, C. B. R.; Piva, M. M.; Rosa, P. F. S.; Adriano, C.; Fisk, Z.; Pagliuso, P. G. Magnetic Properties of the $RAuBi_2$ (R = Ce, Pr, Nd, Gd, Sm) Series of Intermetallic Compounds.*Phys.Procedia*, **2015**,*75*,618-624.https://doi.org/10.1016/j.phpro.2015.12.079.

59. Thamizhavel, A.; Takeuchi, T.; Okubo, T.; Yamada, M.; Asai, R.; Kirita, S.; Galatanu, A.; Yamamoto, E.; Ebihara, T.; Inada, Y.; Settai, R.; Ōnuki, Y. Anisotropic Electrical and Magnetic Properties of $CeTSb_2$ (T=Cu, Au, and Ni) Single Crystals. *Phys. Rev. B.* **2003**, *68 (5)*. 054427.https://doi.org/10.1103/physrevb.68.054427.

60. Kodama, K.; Wakimoto, S.; Igawa, N.; Shamoto, S.; Mizoguchi, H.; Hosono, H. Crystal and Magnetic Structures of the Superconductor $CeNi_{0.8}Bi_2$. *Phys. Rev. B.* **2011**, *83 (21)*. 214512.https://doi.org/10.1103/physrevb.83.214512.

61. Ruszała, P.; Winiarski, M. J.; Samsel-Czekała, M. Dirac-like Band Structure of $LaTESb_2$ (TE = Ni, Cu, and Pd) Superconductors by DFT Calculations. *Comput. Mater. Sci*. **2018**, *154*, 106–110.https://doi.org/10.1016/j.commatsci.2018.07.042.

62. Hase, I.; Yanagisawa, T. Electronic Band Calculation of $LaTSb_2$ (T=Cu,Ag,Au). *Phys. Procedia*. **2014**, *58*, 42–45.https://doi.org/10.1016/j.phpro.2014.09.011.

63. Gautreaux, D. P.; Parent, M.; Karki, A. B.; Young, D. P.; Chan, J. Y. Investigation of the Effect of Ni Substitution on the Physical Properties of $Ce(Cu_{1-x}Ni_x)_ySb_2$. *J. Phys. Condens. Matter*. **2009**, *21 (5)*, 056006. https://doi.org/10.1088/0953-8984/21/5/056006.

64. Muro, Y.; Takeda, N.; Ishikawa, M. Magnetic and Transport Properties of Dense Kondo Systems, $CeTSb_2$ (T=Ni, Cu, Pd and Ag). *J. Alloys Compd.* **1997**, *257 (1–2),* 23–29.https://doi.org/10.1016/s0925-8388(96)03128-3

65. Jung, M. H.; Lacerda, A. H.; Takabatake, T. Magnetic and Transport Properties of the Antiferromagnetic Kondo-Lattice compound $CeNiBi_2$. *Phys. Rev. B.* **2002**, *65 (13)*. 132405.https://doi.org/10.1103/physrevb.65.132405.

66. Adriano, C.; Rosa, P. F. S.; Jesus, C. B. R.; Mardegan, J. R. L.; Garitezi, T. M.; Grant, T.; Fisk, Z.; Garcia, D. J.; Reyes, A. P.; Kuhns, P. L.; Urbano, R. R.; Giles, C.; Pagliuso, P. G. Physical Properties and Magnetic Structure of the intermetallic $CeCuBi_2$ compound. *Phys. Rev. B.* **2014**, *90* (23),235120. .https://doi.org/10.1103/physrevb.90.235120.

67. Buckow, A.; Kupka, K.; Retzlaff, R.; Kurian, J.; Alff, L. Superconducting Epitaxial Thin Films of $CeNixBi_2$ with a Bismuth Square Net Structure. *Appl. Phys. Lett.* **2012**, *101* (16),4760264.https://doi.org/10.1063/1.4760264.

68. Retzlaff, R.; Buckow, A.; Komissinskiy, P.; Ray, S.; Schmidt, S.; Mühlig, H.; Schmidl, F.; Seidel, P.; Kurian, J.; Alff, L. Superconductivity and Role of Pnictogen and Fe Substitution in 112-$LaPd_xPn_2$(Pn=Sb,Bi). *Phys. Rev. B.* **2015,** *91 (10).* 104519.https://doi.org/10.1103/physrevb.91.104519.

69. Thomas, E. L.; Moldovan, M.; Young, D. P.; Chan, J. Y. Synthesis, Structure, and Magneto-Transport of $LnNi_{1-x}Sb_2$ (Ln = Y, Gd−Er). *Chem. Mater.* **2005**, *17 (23),* 5810–5816.https://doi.org/10.1021/cm051196a.

70. Chamorro, J. R.; Topp, A.; Fang, Y.; Winiarski, M. J.; Ast, C. R.; Krivenkov, M.; Varykhalov, A.; Ramshaw, B. J.; Schoop, L. M.; McQueen, T. M. Dirac fermions and possible weak antilocalization in $LaCuSb_2$. *APL Mater.* **2019**, *7*, 121108.https://doi.org/10.1063/1.5124685.

71. APEX2; Bruker AXS Inc.: Madison, WI, 2005.

72. Sheldrick, G. M. A Short History of SHELX. *Acta Crystallogr. A*, **2008**, *64* (1), 112−122.

73. Kresse, G.; Hafner, J. Ab Initio Molecular Dynamics for Liquid Metals. *Phys. Rev. B: Condens.MatterMater.Phys.* **1993**, *47*, 558– 561.https://doi.org/10.1103/physrevb.47.558.

74. Kresse, G.; Hafner, J. Ab Initio Molecular-Dynamics Simulation of the Liquid-Metal-Amorphous-Semiconductor Transition in Germanium. *Phys. Rev. B: Condens. Matter Mater. Phys.* **1994**, *49*, 14251– 14269.https://doi.org/10.1103/physrevb.49.14251.

75. Kresse, G.; Furthmüller, J. Efficiency of Ab-Initio Total Energy Calculations for Metals and Semiconductors Using a Plane-Wave Basis Set. *Comput. Mater. Sci.* **1996**, *6*, 15– 50. https://doi.org/10.1016/0927-0256(96)00008-0.

76. Kresse, G.; Furthmüller, J. Efficient Iterative Schemes for Ab Initio Total-Energy Calculations Using a Plane-Wave Basis Set. *Phys. Rev. B: Condens. Matter Mater. Phys.* **1996**, *54*, 11169–11186.https://doi.org/10.1103/physrevb.54.11169.

77. Perdew, J. P.; Burke, K.; Ernzerhof, M. Generalized Gradient Approximation Made Simple. *Phys. Rev. Lett.* **1996**, *77*, 3865– 3868.https://doi.org/10.1103/physrevlett.77.3865.

78. Monkhorst, H. J.; Pack, J. D. Special Points for Brillouin-Zone Integrations. *Phys. Rev. B: Condens. Matter Mater. Phys.* **1976**, *13*, 5188– 5192. https://doi.org/10.1103/physrevb.13.5188.

79. Kresse, G.; Joubert, D. From Ultrasoft Pseudopotentials to the Projector Augmented-Wave Method. *Phys. Rev. B: Condens. Matter Mater. Phys.* **1999**, *59*, 1758– 1775. https://doi.org/10.1103/physrevb.59.1758

80. Dudarev, S. L.; Botton, G.A.; Savrasov, S. Y.; Humphreys, C. J.; Sutton, A. P. Electron-energy-loss spectra and the structural stability of nickel oxide: An LSDA+U study. *Phys. Rev. B: Condens. Matter Mater. Phys.* **1998**, *57*, 1505– 1509.https://doi.org/10.1103/physrevb.57.1505.

81. Soh, J.-R.; Jacobsen, H.; Ouladdiaf, B.; Ivanov, A.; Piovano, A.; Tejsner, T.; Feng, Z.; Wang, H.; Su, H.; Guo, Y.; Shi, Y.; Boothroyd, A. T. Magnetic Structure and Excitations of the Topological Semimetal $YbMnBi_2$. *Phys. Rev. B.* **2019**, *100* (14), 144431.https://doi.org/10.1103/physrevb.100.144431

82. Tobin, S. M.; Soh, J.-R.; Su, H.; Piovano, A.; Stunault, A.; Alberto Rodriguez-Velamazan, J.; Guo, Y.; Boothroyd, A. T. Magnetic excitations in the topological semimetal $YbMnSb_2$. *Phys. Rev. B.* **2023**, *107*, 195146.https://doi.org/10.1103/PhysRevB.107.195146

83. Zhang, Z.; Guo, Z.; Lin, J.; Sun, F.; Han, X.; Wang, G.; Yuan, W. Effect of Cu Doping on Structure and Physical Properties in the Antiferromagnetic Dirac Semimetal $CaMnBi_2$. *Inorg. Chem.* **2022**, *61* (11), 4592–4597.https://doi.org/10.1021/acs.inorgchem.1c03410.

84. Soh, J.-R.; Manuel, P.; Schröter, N. M. B.; Yi, C. J.; Orlandi, F.; Shi, Y. G.; Prabhakaran, D.; Boothroyd, A. T. Magnetic and Electronic Structure of Dirac Semimetal Candidate $EuMnSb_2$.*Phys.Rev.B.***2019**,*100*(17), 174406.https://doi.org/10.1103/physrevb.100.174406.

85. Marshall, M.; Pletikosić, I.; Yahyavi, M.; Tien, H.-J.; Chang, T.-R.; Cao, H.; Xie, W. Magnetic and Electronic Structures of Antiferromagnetic Topological Material Candidate $EuMg_2Bi_2$.*J.Appl.Phys.***2021**,*129*(3), 035106.https://doi.org/10.1063/5.0035703.

86. Aryal, N.; Li, Q.; Tsvelik, A. M.; Yin, W. Topological Antiferromagnetic Semimetal for Spintronics: A Case Study of a Layered Square-Net System $EuZnSb_2$. *Phys. Rev. B.* **2022**, *106* (23), 235116.https://doi.org/10.1103/physrevb.106.235116.

87. Gofryk, K.; Kaczorowski, D.; Plackowski, T.; Leithe-Jasper, A.; Grin, Y. Magnetic and Transport Properties of Rare-Earth-Based Half-Heusler phases RPdBi: Prospective Systems for Topological Quantum Phenomena. *Phys. Rev. B: Condens. Matter Mater. Phys.* **2011**, *84* (3),035208.https://doi.org/10.1103/PhysRevB.84.035208

88. Ogunbunmi, M. O.; Baranets, S.; Bobev, S. Materials Design, Synthesis, and Transport Properties of Disordered Rare-Earth Zintl Bismuthides with the *Anti*-Th_3P_4 Structure Type. *Dalton Trans.* **2022**, *51* (13), 5227–5238.https://doi.org/10.1039/d2dt00412g.

89. Seibel, E. M.; Xie, W.; Gibson, Q. D.; Cava, R. J. Synthesis, Structure, and Basic Magnetic and Thermoelectric Properties of the Light Lanthanide Aurobismuthides. *Inorg. Chem.* **2016**, *55* (7), 3583–3588.https://doi.org/10.1021/acs.inorgchem.6b00094.

90. Zeng, L.; Franzen, H. F. Crystal Structure of a New Compound Bi_2NdNi. *J. Alloys Compd.* **1998**, *266* (1–2), 155–157.https://doi.org/10.1016/s0925-8388(97)00517-3.

91. Hofmann, W. K.; Jeitschko, W. Ternary Pnictides $MNi_{2-x}Pn_2$ (M ≡ Sr and Rare Earth Metals, Pn ≡ Sb, Bi) with Defect $CaBe_2Ge_2$ and Defect $ThCr_2Si_2$ Structures. *J. Less-common Met.* **1988**, *138* (2), 313–322. https://doi.org/10.1016/0022-5088(88)90119-1.

92. Zelinska, O. Y.; Mar, A. Ternary Rare-Earth Manganese Bismuthides: Structures and Physical Properties of RE_3MnBi_5 (RE = La−Nd) and $Sm_2Mn_3Bi_6$. *Inorg. Chem.* **2008**, *47* (1), 297–305. https://doi.org/10.1021/ic701428p.

93. Hohnke, D.; Parthé, E. Rare-Earth Bismuthides with $D8_8$ and Hf_5Sn_3Cu-Type Structures. *J. Less-common Met.* **1969**, *17* (3), 291–296.https://doi.org/10.1016/0022-5088(69)90146-5.

94. Górnicka, K.; Gutowska, S.; Winiarski, M. J.; Wiendlocha, B.; Xie, W.; Cava, R. J.; Klimczuk, T. Superconductivity on a Bi Square Net in LiBi. *Chem. Mater.* **2020**, *32 (7)*, 3150– 3159, DOI: 10.1021/acs.chemmater.0c00179

95. Major, H. G. ; Fairley, N.; Sherwood, P. M. A.; Linford, M. R.; Terry, J.; Fernandez, V.; Artyushkova, K. Practical guide for curve fitting in x-ray photoelectron spectroscopy.*J.Vac.Sci.Technol. A*., **2020**, *38*, 061203. https://doi.org/10.1116/6.0000377

96. Baltrus, J. P.; Keller, J. M. Rare earth oxides Eu_2O_3 and Nd_2O_3 analyzed by XPS. *Surf. Sci. Spectra*, **2019**, *26*, 014001. https://doi.org/10.1116/1.5085768

97. Haasch, R. T.; Breckenfeld, E.; Martin, L. W. Single Crystal Perovskites Analyzed Using X-ray Photoelectron Spectroscopy: 5. $NdGaO_3$(110). *Surf. Sci. Spectra,* **2014**, *21*, 122–130. https://doi.org/10.1116/11.20140905
98. Haasch, R. T.; Martin, L. W.; Breckenfeld, E. Single Crystal Rare-earth Scandate Perovskites Analyzed Using X-ray Photoelectron Spectroscopy: 2. $NdScO_3$(110). *Surf. Sci. Spectra*, **2014**, *21*,140–148. https://doi.org/10.1116/11.20140907
99. Szytuła, A., Fus, D., Penc, B., Jezierski, A. Electronic structure of RTX (R=Pr, Nd; T=Cu, Ag, Au; X=Ge, Sn) compounds. *J. Alloys Compd.,* **2001**, *317–318,* 340-346. https://doi.org/10.1016/S0925-8388(00)01427-4.
100. Yoshihara, K.; Taylor, J. B.; Calvert, L. D.; Despault, J. G. Rare-earth bismuthides. *J. Less-common Met.* **1975**, *41* (2), 329–337. https://doi.org/10.1016/0022-5088(75)90038-7.
101. Borisenko, S.; Evtushinsky, D.; Gibson, Q.; Yaresko, A.; Koepernik, K.; Kim, T.; Ali, M.; van den Brink, J.; Hoesch, M.; Fedorov, A.; Haubold, E.; Kushnirenko, Y.; Soldatov, I.; Schäfer, R.; Cava, R. J. Time-reversal symmetry breaking type-II Weyl state in $YbMnBi_2$. *Nat. Commun.* **2019**, *10*, 3424. DOI: 10.1038/s41467-019-11393-5.
102. Liu, J.; Hu, J.; Zhang, Q.; Graf, D; Cao, H. B.; Radmanesh, S. M. A.; Adams, D. J.; Zhu, Y. L.; Cheng, G. F.; Liu, X.; Phelan, W. A.; Wei, J.; Jaime, M.; Balakirev, F.; Tennant, D. A.; DiTusa, J. F.; Chiorescu, I.; Spinu, L.; Mao, Z. Q. A magnetic topological semimetal $Sr_{1-y}Mn_{1-y}Sb_2$ (y, z < 0.1). *Nat. Mater*. **2017**, *16,* 905– 910, DOI: 10.1038/nmat4953.
103. Park, J.; Lee, G.; Wolff-Fabris, F.; Koh, Y. Y.; Eom, M. J.; Kim, Y. K.; Farhan, M. A.; Jo, Y. J.; Kim, C.; Shim, J. H.; Kim, J. S. Anisotropic Dirac Fermions in a Bi Square Net of $SrMnBi_2$. *Phys. Rev. Lett.* **2011**, *107*, 126402 DOI: 10.1103/PhysRevLett.107.126402.
104. Cicirello, G.; Wu, K.; Zhang, B. B.; Wang, J. Applying Band Gap Engineering to Tune the Linear Optical and Nonlinear Optical Properties of Noncentrosymmetric Chalcogenides $La_4Ge_3Se_xS_{12-x}$ (x = 0, 2, 4, 6, 8, 10). *Inorg. Chem. Front.* **2021**, *8* (22), 4914–4923.https://doi.org/10.1039/d1qi00879j.
105. Cicirello, G.; Wu, K.; Wang, J. Synthesis, Crystal Structure, Linear and Nonlinear Optical Properties of Quaternary Sulfides $Ba_6(Cu_2X)Ge_4S_{16}$ (X=Mg, Mn, Cd). *J. Solid State Chem.* **2021**, *300*, 122226.https://doi.org/10.1016/j.jssc.2021.122226.
106. Ye, Z.; Bardelli, S.; Wu, K.; Sarkar, A.; Swindle, A.; Wang, J. Synthesis, Crystal Growth, Electronic Properties and Optical Properties of $Y_6IV_{2.5}S_{14}$ (IV=Si, Ge). *Z. Anorg. Allg. Chem.* **2022**, *648* (2),e202100271.http://dx.doi.org/10.1002/zaac.202100271

107. Bardelli, S.; Ye, Z.; Wang, F.; Zhang, B.; Wang, J. Synthesis, Crystal and Electronic Structures, and Nonlinear Optical Properties of $Y_4Si_3S_{12}$. *Z. Anorg. Allg. Chem.* **2022**, *648* (15),e202100388. https://doi.org/10.1002/zaac.202100388.

108. Ji, B.; Wu, K.; Chen, Y.; Wang, F.; Rossini, A. J.; Zhang, B.; Wang, J. $Ba_6(Cu_xZ_y)Sn_4S_{16}$ (Z = Mg, Mn, Zn, Cd, in, Bi, Sn): High Chemical Flexibility Resulting in Good Nonlinear-Optical Properties. *Inorg. Chem.* **2022**, *61* (5), 2640–2651. https://doi.org/10.1021/acs.inorgchem.1c03773

109. Ji, B.; Wang, F.; Wu, K.; Zhang, B.; Wang, J. D^6*versus* d^{10}, Which Is Better for Second Harmonic Generation Susceptibility? A Case Study of $K_2TGe_3Ch_8$ (T = Fe, Cd; Ch = S, Se). *Inorg. Chem.* **2023**, *62* (1), 574–582.https://doi.org/10.1021/acs.inorgchem.2c03852

110. Ji, B.; Pandey, K.; Harmer, C. P.; Wang, F.; Wu, K.; Hu, J.; Wang, J. Centrosymmetric or Noncentrosymmetric? Transition Metals Talking in $K_2TGe_3S_8$(T = Co, Fe). *Inorg. Chem.* **2021**, *60* (14), 10603–10613.https://doi.org/10.1021/acs.inorgchem.1c01149.

111. Jiao, Z.; Quah, J.; Syed, T. H.; Wei, W.; Zhang, B.; Wang, F.; Wang, J. Synthesis, Crystal and Electronic Structures, Linear and Nonlinear Optical Properties, and Photocurrent Response of Oxyhalides $CeHaVIO_4$ (Ha = Cl, Br; VI = Mo, W). *Dalton Trans.* **2024**, *53* (5), 2029–2038. https://doi.org/10.1039/D3DT03640E.

112. Ji, B.; Sarkar, A.; Wu, K.; Swindle, A.; Wang, J. $A_2P_2S_6$ (A = Ba and Pb): A Good Platform to Study the Polymorph Effect and Lone Pair Effect to Form an Acentric Structure. *Dalton Trans.* **2022**, *51* (11), 4522–4531.https://doi.org/10.1039/D1DT04317J.

113. Sangeetha, N. S.; Anand, V. K.; Cuervo-Reyes, E.; Smetana, V.; Mudring, A.-V.; Johnston, D. C. Enhanced Moments of Eu in Single Crystals of the Metallic Helical antiferromagnet $EuCo_{2-y}As_2$. *Phys. Rev. B.* **2018**, *97* (14). https://doi.org/10.1103/physrevb.97.144403.

114. Harmon, B. N.; Freeman, A. J. Spin-Polarized Energy-Band Structure, Conduction-Electron Polarization, Spin Densities, and the Neutron Magnetic Form Factor of Ferromagnetic Gadolinium. *Phys. Rev.* **1974**, *10* (5), 1979–1993. https://doi.org/10.1103/physrevb.10.1979.